Vapor Phase Infiltration of Metal Oxides into Nanoporous Polymers for Organic Solvent Separation Membranes

Emily K. McGuinness,[†,‡] Fengyi Zhang,[#,‡] Yao Ma,[#] Ryan P. Lively[*,#] and Mark D. Losego[*,†]
[†]School of Materials Science and Engineering, [#]School of Chemical and Biomolecular Engineering, Georgia Institute of Technology, Atlanta, GA 30332, USA

Supporting Information

Table of Contents

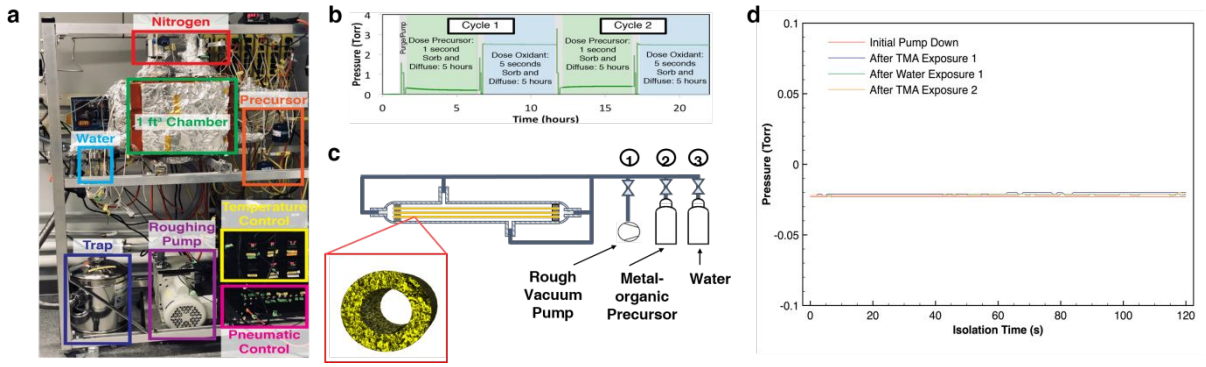

Figure S1. Schematic of vapor phase infiltration (VPI) reactor, process, and integration with membrane module. (a) Custom-built hot walled VPI reactor used for infiltration processes in this work. Reactor is 1 ft^3 in size, allowing for large-scale processing. Reactor is temperature-controlled using custom-built PID controllers. Valves are actuated pneumatically using compressed air and a custom control box. Nitrogen supply is 99.999% purity and is supplied at 250 sccm by a mass flow controller. Precursor bottles and water attachment serve as reservoirs for reactive species. A trap is used prior to a rotary vane roughing pump to reduce the presence of reactive species and byproducts in the pump oil. (b) Chamber pressure (as measured by a Baratron Capacitance Manometer) as a function of time. The steps in the infiltration process for PIM-1 membranes are labeled at their corresponding times. Initially, the chamber is purged and pumped for a length of time sufficient to remove residual water. Then a precursor is dosed and allowed to sorb and diffuse for a set amount of time. The chamber is then purged and pumped again before dosing an oxidant (in this case water) and again allowing time for water to sorb and diffuse. The process is then repeated in a second cycle but could be repeated for any number more. (c) Illustration of conducting VPI in a hollow fiber membrane module. All ports of a typical membrane module are temporally connected to a rough vacuum pump, a metal-organic precursor container, and a water container. The temperature of all tubes and modules are maintained by heating pads or a water bath. By switching the valves, membranes in the module can be evacuated (open valve 1 but close valve 2 and 3), infiltrated with metal-organic precursors (open valve 2 but close valve 1 and 3) or infiltrated with water vapor (open valve 3 but close valve 1 and 2). After infiltration, pumps and reactant containers can be disassembled. The module containing hybrid membranes can then be integrated into separation processes. (d) No significant byproduct release is observed in the two minute isolation step following the five minute purge and five minute pump down portion of the VPI process after each exposure, as measured by a Baratron Capacitance Manometer sensitive to 0.001 Torr.

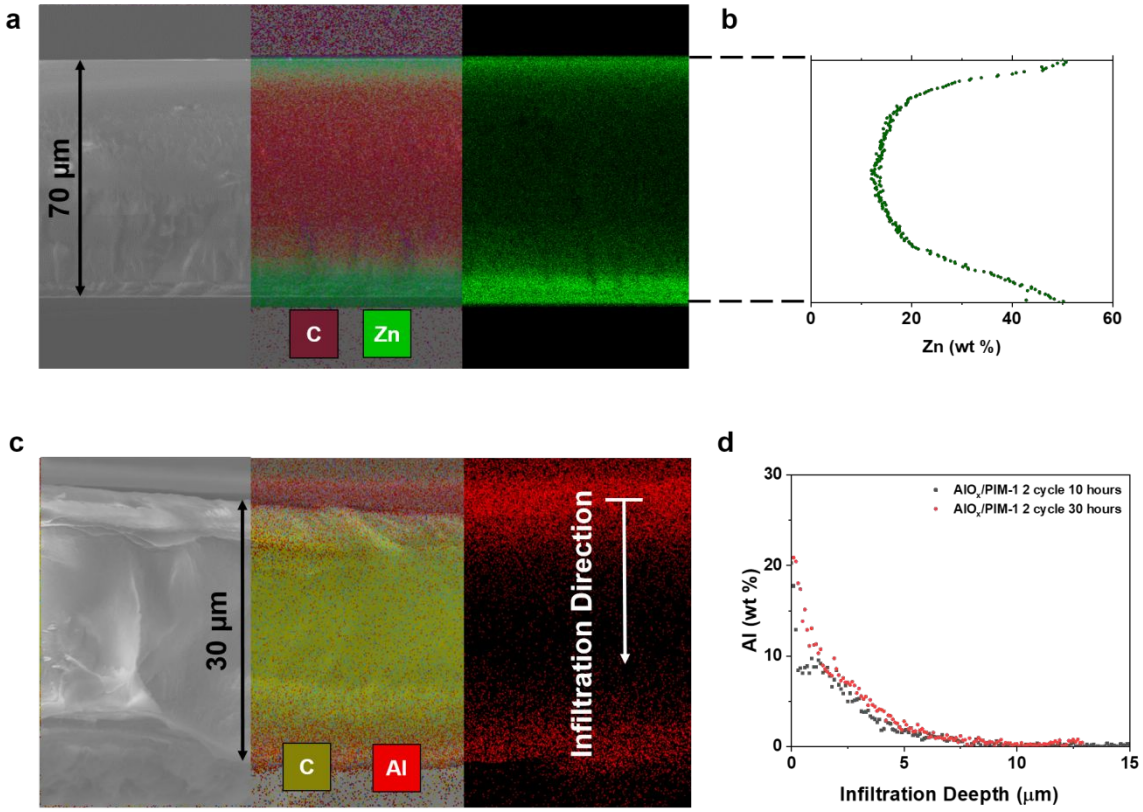

Figure S2. Infiltration depth as a function of infiltration cycles and exposure time. (a) EDX elemental map of a defect-free PIM-1 membrane of 70 µm thickness after 10 cycles of infiltration of ZnO_x with a exposure time of 2 hours at 90 °C. (b) Zinc loading profile across the membrane shown in Figure S2a. (c) EDX elemental map of a defect-free PIM-1 membrane of 30 µm thickness after 2 cycles of infiltration of AlO_x with an exposure time of 10 hours at 90 °C; (d) Infiltration depth of aluminum into the 30-µm PIM-1 membranes as a function of exposure time. The loading of metal atoms reaches a maximum on the edges of the membrane and decreases into the center of the membrane due to diffusion limitations. Longer exposure times can increase the infiltration depth. Metal oxide loading amounts and depths also depend on membrane morphology. Dense membranes with low free volume have large characteristic mass transfer lengths and require long diffusion times to achieve full infiltration. Since it is challenging to fully infiltrate dense thick PIM-1 membranes in reasonable timeframes, membranes with a thin PIM-1 selective layer (e.g., thin film composite [TFC] and hollow fiber membranes) are used in the following experiments to ensure thorough infiltration of the metal oxide.

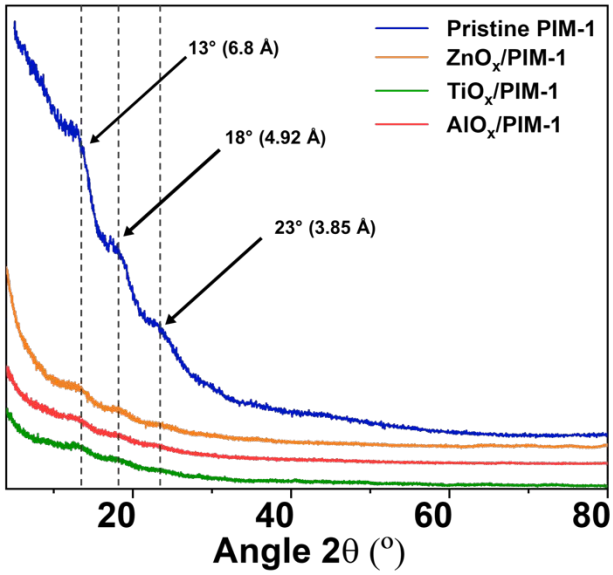

Figure S3. XRD patterns of pristine PIM-1, ZnO_x/PIM-1, TiO_x/PIM-1, and AlO_x/PIM-1. Characteristic peaks of PIM-1 at 13°, 18°, and 23° indicate the interlayer spacing of 6.8 Å, 4.92 Å, and 3.85 Å. These peaks were also observed at the identical position in ZnO_x/PIM-1, TiO_x/PIM-1, and AlO_x/PIM-1, which suggests that the infiltrated metal oxides do not interrupt the nanoporous structures of PIM-1. None of the characteristic peaks corresponding to the crystal structures of metal oxides were found.

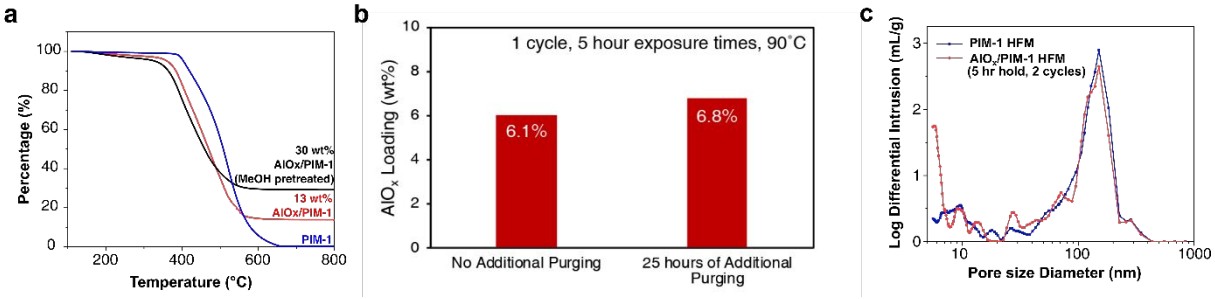

Figure S4. Supplementary experiments exploring the process-structure relationships of PIM-1 vapor phase infiltrated with TMA / H_2O. (a) TGA data demonstrating that a methanol pretreatment increases metal oxide loading. PIM-1 hollow fiber membranes (HFMs) with and without methanol pretreatment were VPI treated with 2 cycles of TMA/H_2O with 5-hour exposure times at 90 °C. Methanol pretreatment increases the AlO_x loading from 13 weight percent to 30 weight percent. **(b)** Long-duration purging experiments. PIM-1 hollow fiber membranes were methanol pre-treated, dried, and VPI treated with 1 cycle of TMA/H_2O with 5-hour exposure times at 90˚C. For one membrane ("no additional purging"), the typical procedure of N_2 purging five minutes and pumping five minutes was followed prior to the final 5-hour water vapor exposure. For the other membrane, an additional 25-hour purge step was placed between TMA and water vapor exposures to determine whether TMA would diffuse out of the membrane during this time. Both methods resulted in similar weight percent loadings of AlO_x in PIM-1. This result suggests that the binding state between TMA and PIM-1 is semi-permanent and does not significantly desorb during the VPI process. (c) Mesoporosity and macroporosity of pristine PIM-1 and AlO_x/PIM-1 hollow fiber membranes explored by mercury porosimetry.

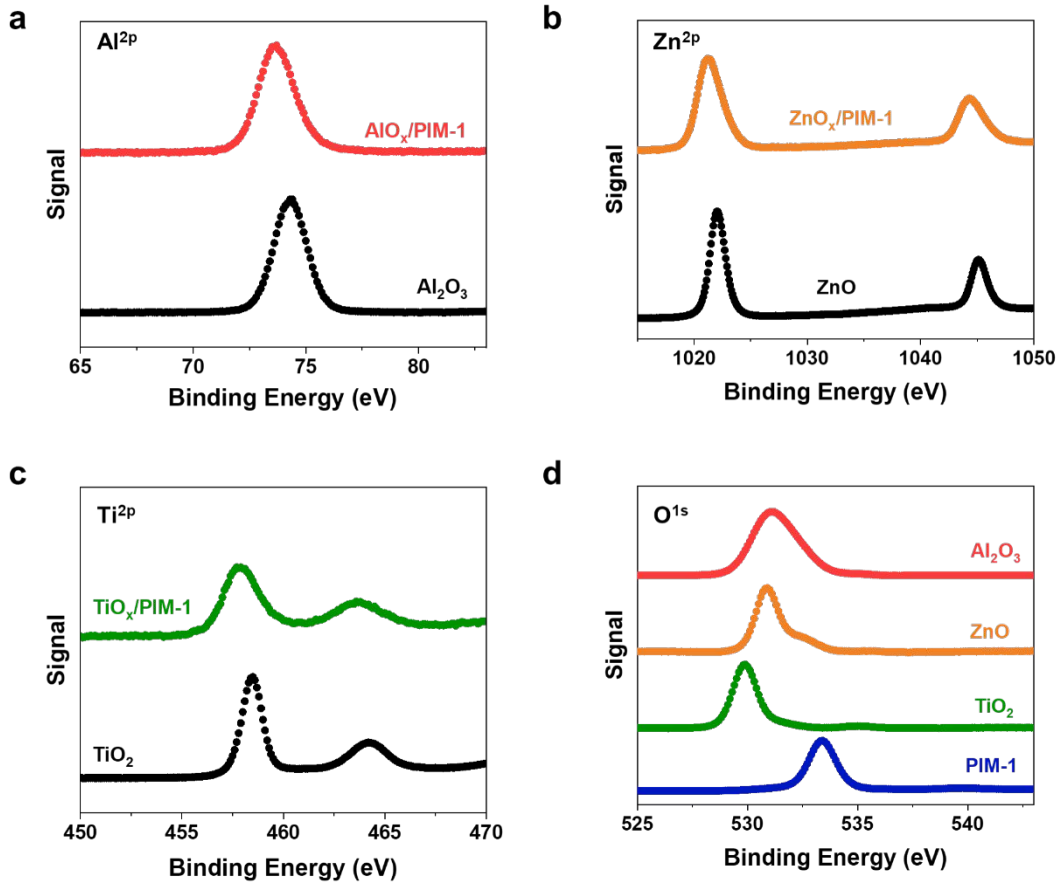

Figure S5. Supplementary XPS spectra. (a) Al^{2p} spectra of Al_2O_3 and AlO_x/PIM-1; (b) Zn^{2p} spectra of ZnO and ZnO_x/PIM-1; (c)Ti^{2p} spectra of TiO_2 and TiO_x/PIM-1; (d) O^{1s} spectra of Al_2O_3, ZnO, TiO_2 and pristine PIM-1. Details of sample preparation and peak calibration are discussed in the experimental section. 2p electrons of the metal atoms in the hybrid material exhibit slightly lower binding energy and wider peaks than those in the reference metal oxide produced by atomic layer deposition (Figure S5a, b, and c). The subtle difference may suggest structure differences between metal oxides under different confinement conditions, which requires further investigation in the future.

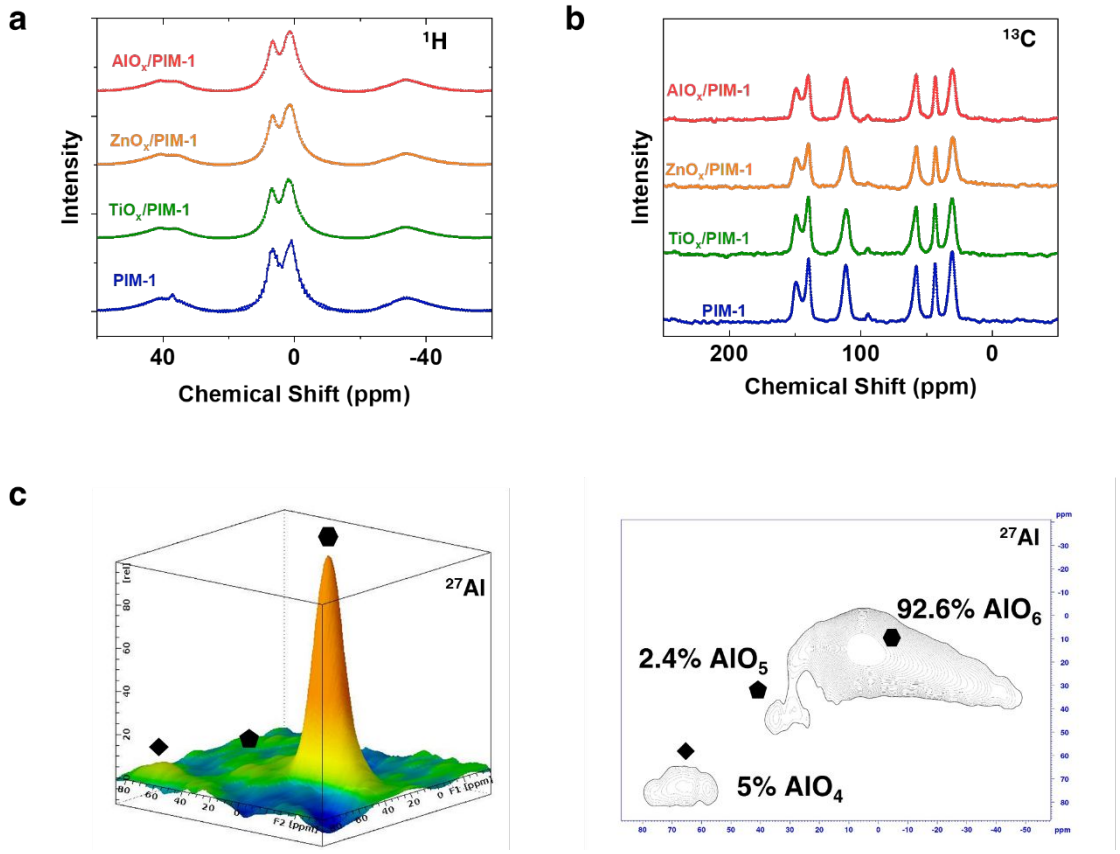

Figure S6. Solid-state ^{1}H, ^{13}C and ^{27}Al NMR. (a) Solid-state ^{1}H NMR spectra of pristine PIM-1, ZnO$_x$/PIM-1, TiO$_x$/PIM-1, and AlO$_x$/PIM-1; (b) solid-state ^{13}C NMR spectra of pristine PIM-1, ZnO$_x$/PIM-1, TiO$_x$/PIM-1, and AlO$_x$/PIM-1; (c) solid-state ^{27}Al NMR spectra of AlO$_x$/PIM-1. All these samples exhibit identical ^{13}C and ^{1}H signals, which indicates the identical chemical environments of carbon and hydrogen atoms. PIM-1 powders used for NMR were obtained via grinding PIM-1 hollow fiber membranes. All PIM-1/metal oxide hybrids are infiltrated twice with 5-hour exposure time. In AlO$_x$/PIM-1, 92.6% of infiltrated aluminum atoms take octahedral coordination, which is hypothetically favored for the AlO$_x$ nanostrand growth within tortuous micropores of the PIM-1 skeleton.

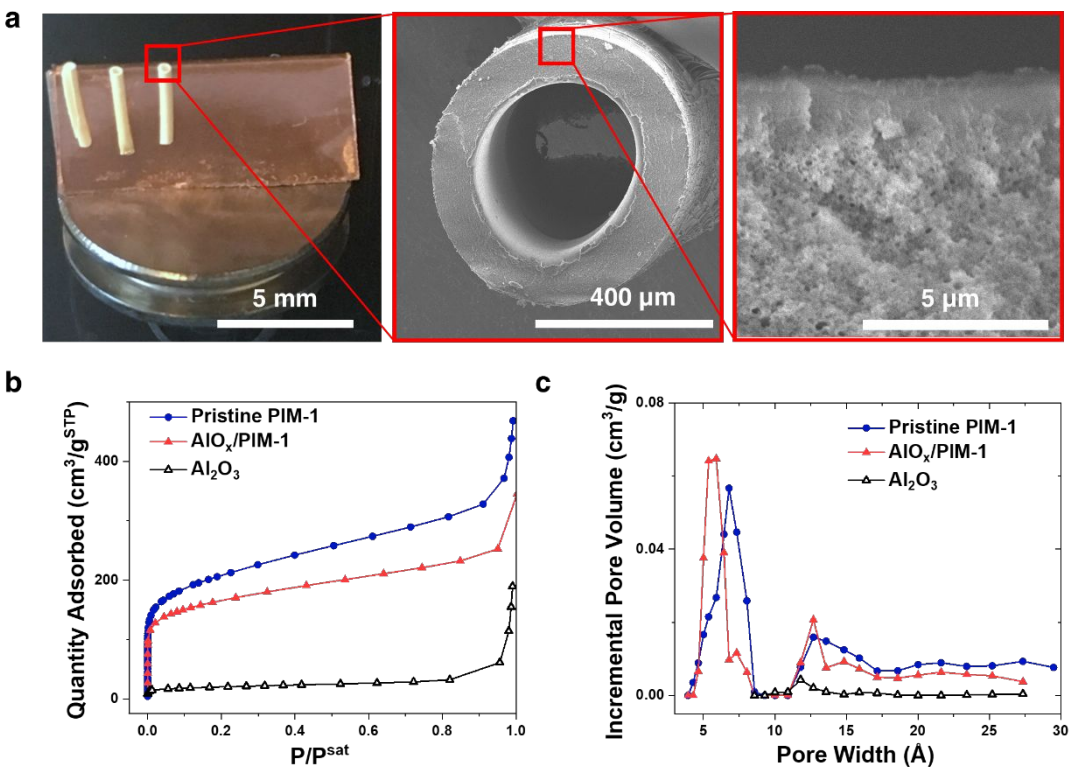

Figure S7. Alumina hollow fiber membrane obtained by annealing AlO_x/PIM-1 hybrid hollow fiber membranes in air (900 °C). Heat treating in air combusts the polymer and leaves just an AlO_x nanoporous structure. (a) Photographs and SEM images of the alumina hollow fiber membrane after burn out; (b) cryogenic nitrogen physisorption of these alumina hollow fiber membranes compared with that of pristine PIM-1 hollow fiber membranes and AlO_x/PIM-1 hollow fiber membranes; (c) pore size distribution of alumina hollow fiber membranes compared that of pristine PIM-1 hollow fiber membranes and AlO_x/PIM-1 hollow fiber membranes. The intact alumina hollow fiber membrane indicates the thorough infiltration of metal oxide into PIM-1 hollow fiber membranes. The porosity exhibited by the alumina hollow fiber membrane is consistent with our hypothesis that metal oxide nanostrands reside in the micropores of PIM-1, which is a porous template. The reduced porosity is likely due to sintering of the structure during heating.

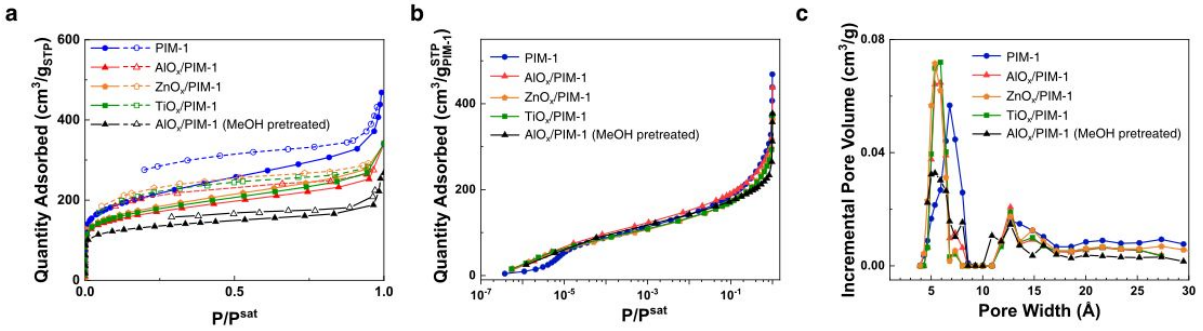

Figure S8. Cryogenic nitrogen physisorption and pore size distribution calculated based on N_2 DFT model. (a) Cryogenic nitrogen physisorption isotherms with both adsorption (solid symbols) and desorption (hollow symbols) parts, (b) isotherms normalized by the weight of PIM-1, and (c) pore size distribution calculated using N_2 DFT model. Infiltrated metal oxide reduces the size of micropores created by PIM-1 backbones. Higher metal oxide loading results in a further reduction of pore sizes. To determine how the entanglement of metal oxides with PIM-1 molecules influenced membrane swelling, cryogenic nitrogen sorption isotherms were created. In the resulting curves (Fig. 3c), pristine PIM-1 hollow fiber membranes show their typical dual-mode sorption behavior: Langmuir-type (flat) sorption behavior in the low pressure region due to nitrogen physisorption into micropores and Henry-type (linear) behavior at higher pressures ($p/p^{sat} > 0.2$) associated with nitrogen induced swelling. Importantly, the hybrid membranes still possess the characteristically high initial nitrogen uptake of pristine PIM-1 membranes. The hybrid membranes exhibit earlier nitrogen uptake in the low-pressure region as a result of the reduced micropores. The high initial sorption behavior of PIM-1 is just one of many attributes that make it an attractive membrane material. Additionally, hybrid PIM-1 membranes all exhibit a reduction in swelling and a more ideal (flat) Langmuir sorption behavior. The degree of swelling reduction is consistent with the metal oxide loading. AlO_x/PIM-1 hybrid membranes pre-treated with methanol have the highest metal oxide loadings and accordingly show nearly ideal (flat) Langmuir sorption (until $p/p^{sat} > 0.8$).

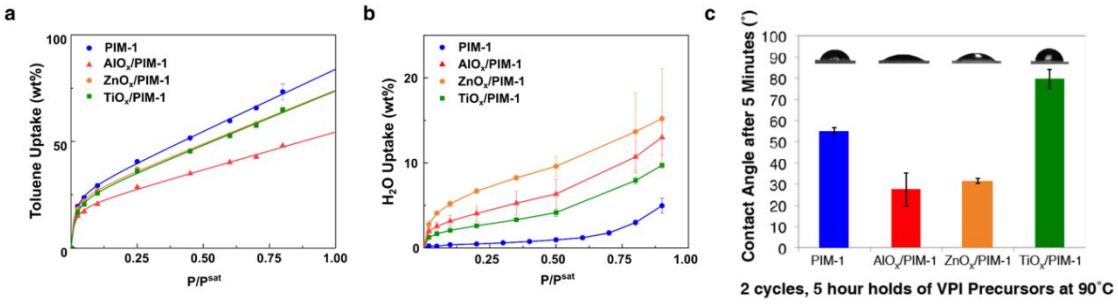

Figure S9. Influence of interpenetrating metal oxide networks on the interaction between guest molecules (toluene and water) and PIM-1 membranes. (a) Toluene swelling reduction. A reduction in swelling is observed in the toluene adsorption isotherms measured at 25 °C. The toluene isotherms can be well fitted by dual-mode sorption equations, which is a combination of Langmuir-type adsorption and Henry-type sorption. By comparing the change in the contribution of Henry-type sorption, we found that the toluene-induced swelling in AlO_x/PIM-1 has been reduced by 39%. This trends reveal that the interpenetrating metal oxide networks protect PIM-1 membranes from swelling while preserving their vital membrane characteristics. (b) H_2O sorption isotherms measured at 25 °C. While pristine PIM-1 is hydrophobic, the metal-oxide-infiltrated PIM-1 hollow fiber membranes show significantly higher water uptake. This increase in water molecule affinity results from additional adsorption sites provided by the interpenetrating metal oxide networks. (c) The increase in hydrophilicity for ZnO_x and AlO_x/PIM-1 membranes is further supported by contact angle measurements. TiO_x membranes, however, exhibit a more hydrophobic contact angle. This may be due to increases in surface roughness on the PIM-1 membranes. Generally, the more hydrophilic nature of ZnO_x and AlO_x/PIM-1 membranes may provide a pathway for the use of PIM-1 based membranes in aqueous separations.

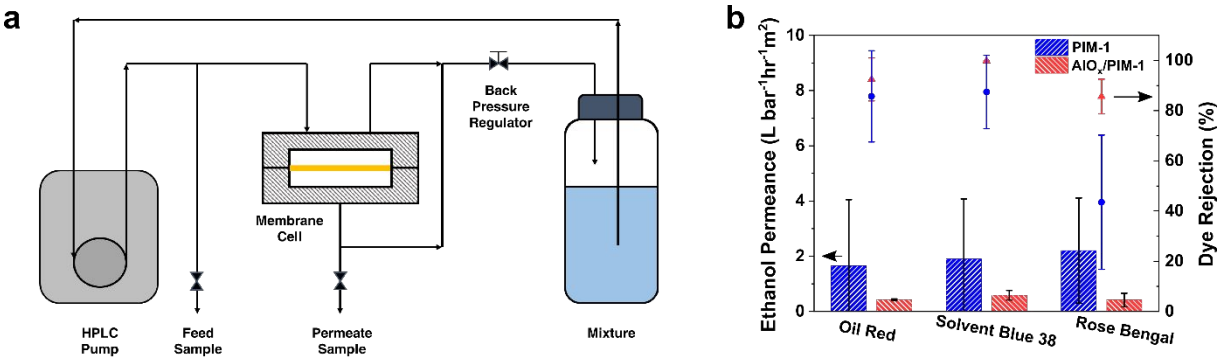

Figure S10. Supplementary organic solvent nanofiltration data. (a) Cross-flow organic solvent permeation system. An HPLC pump delivers pressurized mixture solution into the feed side of the membrane cell. The feed solution makes contact with the membrane and then flows through the backpressure regulator into the mixture container. Permeate is directed by a three-way valve into the mixture container or a sampling vial. Feed solution circulates inside the feed-side chamber of the membrane cell, disturbing the boundary layer near the membrane. Although a flat membrane cell is illustrated here, hollow fiber membrane modules can also be tested in this setup. (b) Dye rejection in ethanol by PIM-1 and AlO_x/PIM-1 hollow fiber membranes. Owing to stronger affinity to untreated PIM-1, bulkier Rose Bengal (973.67 g/mol) is retained less than Solvent Blue 38 (782.18 g /mol) and Oil Red (408.505 g/mol). The deviation from polystyrene retention curve is attributed to the strong interactions between dye molecules and PIM-1. In contrast, AlO_x/PIM-1 membranes achieve more than 80% rejection for all three dyes, indicating the infiltrated metal oxide interrupts the interaction between the dye molecules and the membrane.

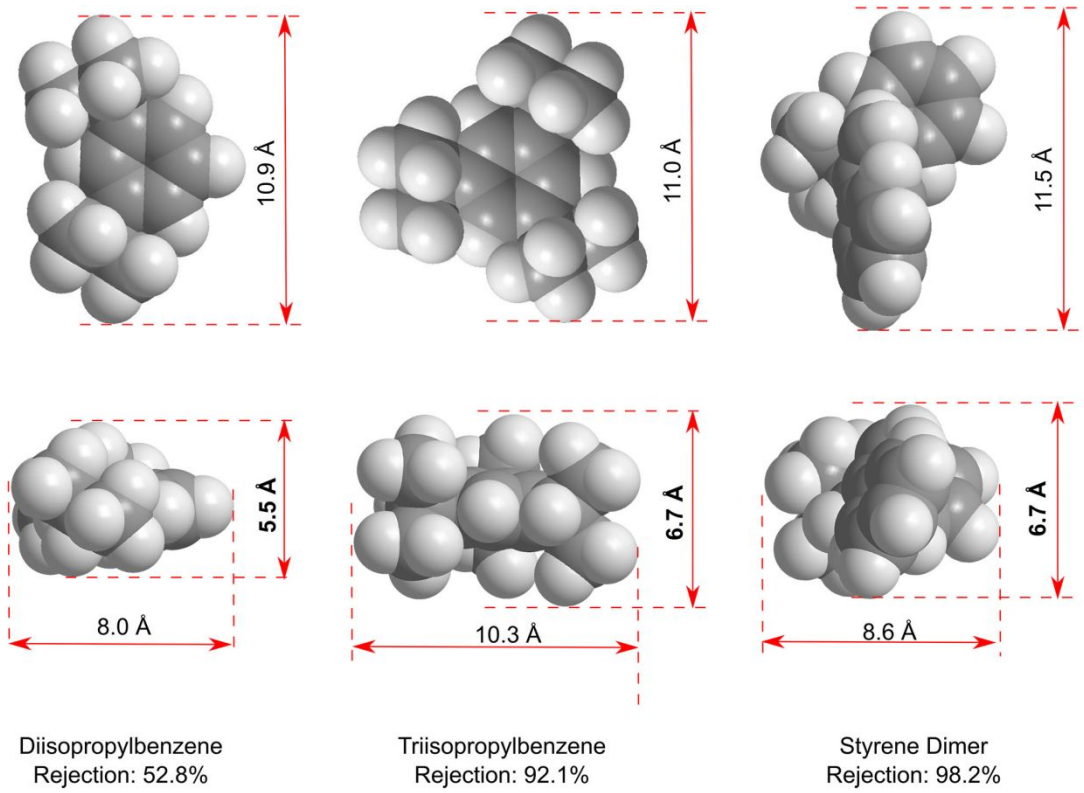

Figure S11. Size-based molecular sieving effects of the AlO_x/PIM-1 hybrid membrane. Space filling models of diisopropylbenzene, triisopropylbenzene, and styrene dimer are generated by Chem3D (ChambridgeSoft). The space occupied by each atom is defined by 100% van der Waals radii. The configuration of each molecule possesses the minimized steric energy, which is optimized by MM2 calculation. The rejection rates of these marker solutes exhibit size-based molecular sieving effects within the AlO_x/PIM-1 hybrid membrane. Diisopropylbenzene with critical diameter (5.5 Å) smaller than AlO_x/PIM-1 micropores (~ 6 Å) permeates with less restriction (rejection = 52.8%), while triisopropylbenzene and styrene dimer with larger critical diameters (6.7 Å) are mostly rejected (rejection > 90%).

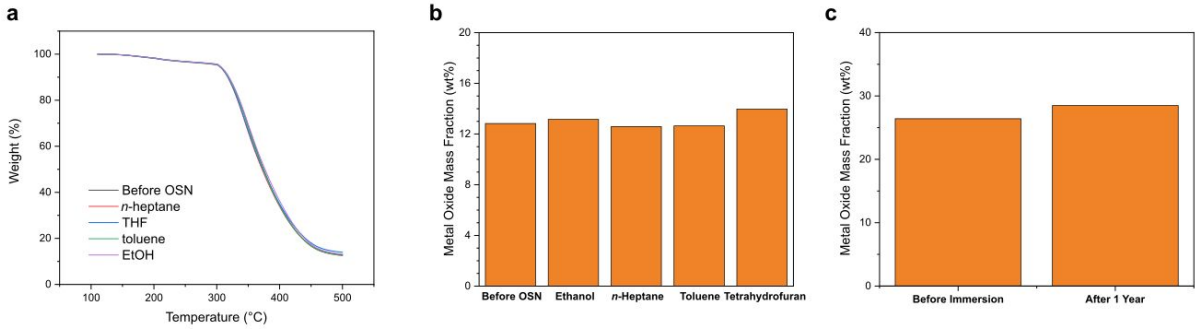

Figure S12. The infiltrated metal oxide networks retain the majority of their inorganic component during the organic solvent separation processes. (a) Thermogravimetric analysis curves of free-standing AlO_x/PIM-1 hollow fiber membranes with different operation histories (before use in organic solvent nanonfiltration and after 1 week of continuous OSN in n-heptane, tetrahydrofuran, toluene, or ethanol). (b) The weight percent loading of the inorganic component of AlO_x/PIM-1 freestanding hollow fiber membranes after 1-week of continuous organic solvent separation in n-hexane, ethanol, toluene, and tetrahydrofuran. (c) The change in weight percent loading of the inorganic component in AlO_x/PIM-1 freestanding hollow fiber membranes after 1-year of immersion in tetrahydrofuran.

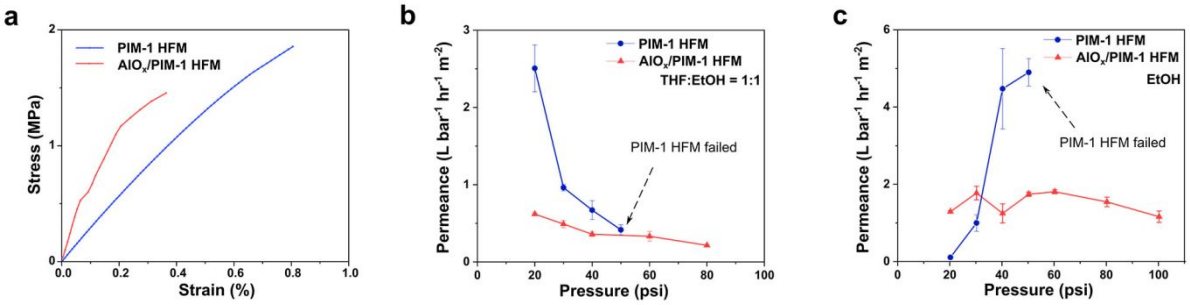

Figure S13. Mechanical stability of free-standing PIM-1 hollow fiber membranes and AlO_x/PIM-1 (2 cycles of infiltration of TMA and H_2O with 5 hour exposure times) hollow fiber membranes. (a) Stress-strain curves of the dry hollow fiber membranes. The AlO_x/PIM-1 exhibit a higher modulus of elasticity but smaller strength at break and strain at break, which indicates that the AlO_x/PIM-1 are stiffer and more brittle than pristine PIM-1 hollow fiber membranes. (b) Mechanical stability of pristine and hybrid hollow fiber membranes in the equal molar mixture of tetrahydrofuran and ethanol. Pristine PIM-1 hollow fiber membranes exhibit high permeance due to swelling and rupture at 3.45 bar while AlO_x/PIM-1 hollow fiber membranes exhibit stable permeance until delaminated from the swollen epoxy sealing at 5.52 bar (c) Mechanical stability in ethanol. Pristine PIM-1 hollow fiber membranes exhibit high permeance due to swelling and rupture at 3.45 bar while AlO_x/PIM-1 hollow fiber membranes exhibit stable permeance until delaminated from the swollen epoxy sealing at 6.89 bar.

Calculation of Osmotic Pressure of Toluene Enrichment

The feed mixture consists of 90 % toluene, 5% triisopropylbenzene, and 5% diisopropylbenzene. Toluene is treated as the main component (denoted as component 1) and the other components are treated as the dilute components (denoted as component 2, collectively). We assume the activity coefficient of toluene to be one. In the case where the permeate is 97% toluene (the experimental data at 40 bar transmembrane pressure), osmotic pressure can be calculated as following.

The osmotic pressure can be defined as:

$$\boldsymbol{\pi = -\frac{RT}{\hat{V}_1}\left(\frac{\gamma_{1,permeate} x_{1,permeate}}{\gamma_{1,retentate} x_{1,retentate}}\right) = 16.1\ bar}$$